

Chemical-Shift Imaging Utilizing the Positional Shifts Along the Readout Gradient Direction

Maria I. Altbach*, Theodore P. Trouard, Rik Van de Walle, Rebecca J. Theilmann, Eric Clarkson, Harrison H. Barrett, and Arthur F. Gmitro

Abstract—In this work, we describe a method that uses the linear phase acquired during the readout period due to chemical shift to generate individual magnetic resonance (MR) images of chemically shifted species. The method utilizes sets of Fourier (or k -space) data acquired with different directions of the readout gradient and a postprocessing algorithm to generate chemical shift images. The methodology is developed for both Cartesian data acquisition and for radial data acquisition. The method is presented here for two chemically shifted species but it can be extended to more species. In this work, we present the theory, show the results in phantoms and in human images, and discuss the artifacts and signal-to-noise ratio of the images obtained with the technique.

Index Terms—Chemical shift, lipid and water, radial MRI, 2-D Fourier MRI.

I. INTRODUCTION

IMAGES in clinical magnetic resonance imaging (MRI) are typically from a combination of two species (i.e., water and lipid) that resonate at different frequencies. The difference in resonance frequency is known as the chemical shift. In MRI, a linear phase is accumulated for the off-resonance species during the acquisition of data. This results in a misregistration (i.e., spatial shift) of the off-resonance species in the reconstructed image in the direction of the readout gradient [1]–[4]. Chemical-shift selective imaging is often used to overcome misregistration errors or when identification of the individual species is desired. Several methods have been developed for chemical-shift imaging. Images of a specific species can be obtained by suppressing the signal of the other species via chemical-shift selective saturation [5]–[9], inversion recovery [10]–[13], dif-

fusion weighting [14], [15], or any combination of the above [16]–[18]. Chemical-shift imaging can also be achieved by collecting multiple data sets using sequence timing parameters to control the phase difference between species. This technique, first proposed by Dixon [19] and further developed by others [20]–[35], is commonly referred to as the Dixon method. Chemical-shift images can also be obtained from localized spectra. Typically, phase encoding gradients are used in two (or three) directions to provide spatial information of the object in two (or three) dimensions and spectral information is encoded in the collected time-domain signal [36]–[42]. Time-varying readout gradients can also be used to obtain spatial/spectral information in two or three dimensions [43]–[48]. Spatial/spectral imaging methods are useful when several species are present, but are time consuming if high-spatial resolution images are required.

Despite the existing methods, chemical-shift imaging is still a subject of current investigation. In clinical MRI, it is important to have a reliable technique that can yield true fat and water images within a reasonable imaging time. In this paper, we describe a method that uses the additional linear phase acquired during the readout period due to chemical shift to generate individual images of chemically shifted species. A method for separating chemically shifted species based on similar principles was described in 1984 by Axel *et al.* for Cartesian data [49]. The formalism is developed herein for Cartesian and radial data. The method utilizes multiple data sets acquired with different orientations of the readout gradient and a simple postprocessing algorithm to generate images of the individual chemically shifted species. In this work, we focus on imaging two chemically shifted species, but the formalism can be extended to additional n species. The chemical-shift separation method is demonstrated in phantoms and in a human head.

II. THEORY

A general expression for the Fourier domain (or k -space) data of a two-dimensional object, $f(\underline{r})$, is given by

$$F(\underline{k}) = \int f(\underline{r})e^{-i2\pi\underline{k}\cdot\underline{r}} d\underline{r} \quad (1)$$

where \underline{k} and \underline{r} are the coordinate vectors in Fourier and in object space, respectively. In MRI, k -space is measured as a function of time and the MR signal is given by

$$\begin{aligned} S_\omega(\underline{k}(t)) &= \int f_\omega(\underline{r})e^{-i\omega t}e^{-i2\pi\underline{k}(t)\cdot\underline{r}} d\underline{r} \\ &= F_\omega(\underline{k}(t))e^{-i\omega t} \end{aligned} \quad (2)$$

where $f_\omega(\underline{r})$ represents the signal intensity of a thin-slice volume as a function of position for a species resonating at a

Manuscript received September 28, 2000; revised August 12, 2001. This work was supported by the National Institutes of Health (NIH) under Grant HL-03528, HL-48206 and Grant CA-52643 and by a grant from the Flinn Foundation. The work of R. Van de Walle was supported by the Fund for Scientific Research (FWO, Belgium). The Associate Editor responsible for coordinating the review of this paper and recommending its publication was X. Hu. Asterisk indicates corresponding author.

*M. I. Altbach is with the Department of Radiology, P.O. Box 245067, University of Arizona, Tucson, AZ 85724-5067 USA (e-mail: maltbach@u.arizona.edu).

T. P. Trouard is with the Department of Radiology, University of Arizona, Tucson, AZ 85724-5067 USA.

R. Van de Walle is with the Department of Radiology, University of Arizona, Tucson, AZ 85724-5067 USA. He is also with the Department of Electronics and Information Systems, Ghent University, B-9000 Ghent, Belgium.

R. J. Theilmann is with the Optical Sciences Center, University of Arizona, Tucson, AZ 85724 USA.

E. Clarkson, H. H. Barrett, and A. F. Gmitro are with the Department of Radiology, University of Arizona, Tucson, AZ 85724-5067 USA. They are also with the Optical Sciences Center, University of Arizona, Tucson, AZ 85724 USA.

Publisher Item Identifier S 0278-0062(01)10000-5.

frequency ω and includes the effects of spin density, longitudinal and transverse relaxation times, and the pulse-sequence dependent timing parameters. The k -space trajectory, $\underline{k}(t)$, is defined by the integral of the readout gradient, $\underline{G}(t)$

$$\underline{k}(t) = \frac{\gamma}{2\pi} \int_{t_o}^t \underline{G}(t') dt' \quad (3)$$

where γ is the gyromagnetic ratio and t_o is the starting time of the readout gradient.

For a sample consisting of two chemically shifted species, one of which is on-resonance ($\omega = 0$), the MRI k -space data are the sum of the k -space data of the individual species

$$S(\underline{k}(t)) = \sum_{\omega} S_{\omega}(\underline{k}(t)) = F_o(\underline{k}(t)) + F_{\omega}(\underline{k}(t))e^{-i\omega t}. \quad (4)$$

If we assume a constant readout gradient, G_{readout} , and adjust the time axis such that $\underline{k} = 0$ at $t = 0$, then any k -space point during the readout period is given by

$$k_{\text{readout}} = \frac{\gamma}{2\pi} G_{\text{readout}} t. \quad (5)$$

We can rewrite (4) as follows:

$$S(\underline{k}(t)) = F_o(\underline{k}(t)) + F_{\omega}(\underline{k}(t))e^{-i2\pi \frac{\omega}{\gamma G_{\text{readout}}} k_{\text{readout}}}. \quad (6)$$

If the linear phase shift in k -space due to chemical shift is expressed in terms of the positional shift in image space, Δ , where

$$\Delta = \frac{\omega}{\gamma G_{\text{readout}}} \quad (7)$$

a final expression for the k -space data of two chemically shifted species is given by

$$S(\underline{k}(t)) = F_o(\underline{k}(t)) + F_{\omega}(\underline{k}(t))e^{-i2\pi \Delta k_{\text{readout}}}. \quad (8)$$

The image reconstructed via Fourier transformation of (8) is the sum of the on-resonance species and the chemically shifted species spatially offset by Δ in the readout direction.

We now describe an algorithm to separate the k -space data of the two chemically shifted species, $F_o(\underline{k}(t))$ and $F_{\omega}(\underline{k}(t))$, when data are acquired with different orientations of the readout gradient. Two cases will be considered: 1) Data acquired radially such as data obtained with radial (projection reconstruction) MRI and 2) data acquired on a Cartesian grid such as data obtained with conventional two-dimensional (2-D) Fourier MRI. For the radial data, we will use two measurements of $S(\underline{k}(t))$ to solve for $F_o(\underline{k}(t))$ and $F_{\omega}(\underline{k}(t))$. For Cartesian data, we will use four measurements of $S(\underline{k}(t))$. The need of four measurements is to reduce some of the image artifacts previously seen in the method reported by Axel *et al.* (see Section V). For simplicity, we drop the explicit time dependence of \underline{k} in the following equations.

A. Forward Problem

For radial data, $k_{\text{readout}} = k_{\rho}$, i.e., the coordinate along a k -space radial line at an angle θ . For an MRI measurement with a readout gradient of positive polarity

$$S_{+\rho}(\underline{k}) = F_o(\underline{k}) + F_{\omega}(\underline{k})e^{-i2\pi k_{\rho} \Delta}. \quad (9)$$

If we switch the polarity of the readout gradient, then

$$S_{-\rho}(\underline{k}) = F_o(\underline{k}) + F_{\omega}(\underline{k})e^{i2\pi k_{\rho} \Delta}. \quad (10)$$

For radial data, Δ is the positional shift along each projection due to chemical shift. We can express (9) and (10) in matrix form

$$\begin{bmatrix} S_{+\rho}(\underline{k}) \\ S_{-\rho}(\underline{k}) \end{bmatrix} = \begin{bmatrix} 1 & e^{-i2\pi k_{\rho} \Delta} \\ 1 & e^{i2\pi k_{\rho} \Delta} \end{bmatrix} \begin{bmatrix} F_o(\underline{k}) \\ F_{\omega}(\underline{k}) \end{bmatrix}. \quad (11)$$

For Cartesian data, k_{readout} can be equal to k_x or k_y , i.e., the readout gradient can have two orthogonal orientations in the imaging plane. If we acquire four sets of data using the x , $-x$, y , and $-y$ directions for G_{readout} , the data expressed in matrix form are

$$\begin{bmatrix} S_{+x}(\underline{k}) \\ S_{-x}(\underline{k}) \\ S_{+y}(\underline{k}) \\ S_{-y}(\underline{k}) \end{bmatrix} = \begin{bmatrix} 1 & e^{-i2\pi k_x \Delta} \\ 1 & e^{i2\pi k_x \Delta} \\ 1 & e^{-i2\pi k_y \Delta} \\ 1 & e^{i2\pi k_y \Delta} \end{bmatrix} \begin{bmatrix} F_o(\underline{k}) \\ F_{\omega}(\underline{k}) \end{bmatrix}. \quad (12)$$

B. Inverse Solution

To find a solution for $F_o(\underline{k})$ and $F_{\omega}(\underline{k})$ it is easier to express (11) and (12) in general operator form

$$\hat{S} = \mathbf{H}\hat{F}. \quad (13)$$

\hat{F} can be solved by inverting (13). The generalized pseudoinverse solution [50] is given by

$$\hat{F} = \lim_{\kappa \rightarrow 0^+} (\mathbf{H}^{\dagger} \mathbf{H} + \kappa \mathbf{I})^{-1} \mathbf{H}^{\dagger} \hat{S} \quad (14)$$

where the operator \mathbf{H}^{\dagger} is the adjoint of the operator \mathbf{H} and \mathbf{I} is the identity operator. For the radial case, the operator $(\mathbf{H}^{\dagger} \mathbf{H})^{-1}$ is

$$(\mathbf{H}^{\dagger} \mathbf{H})^{-1} = \frac{\begin{bmatrix} 2 & -m_p \\ -m_p & 2 \end{bmatrix}}{4 - m_p^2} \quad (15)$$

where

$$m_p = 2 \cos(k_{\rho} \Delta). \quad (16)$$

Thus, the solution to (11) is

$$\begin{bmatrix} F_o(\underline{k}) \\ F_{\omega}(\underline{k}) \end{bmatrix} = \frac{1}{4 - m_p^2} \begin{bmatrix} 2 & -m_p \\ -m_p & 2 \end{bmatrix} \times \begin{bmatrix} 1 & 1 \\ e^{i2\pi k_{\rho} \Delta} & e^{-i2\pi k_{\rho} \Delta} \end{bmatrix} \begin{bmatrix} S_{+\rho}(\underline{k}) \\ S_{-\rho}(\underline{k}) \end{bmatrix}. \quad (17)$$

For the Cartesian case, the operator $(\mathbf{H}^{\dagger} \mathbf{H})^{-1}$ is

$$(\mathbf{H}^{\dagger} \mathbf{H})^{-1} = \frac{\begin{bmatrix} 4 & -m_c \\ -m_c & 4 \end{bmatrix}}{16 - m_c^2} \quad (18)$$

where

$$m_c = 2 \cos(k_x \Delta) + 2 \cos(k_y \Delta). \quad (19)$$

Thus, a solution to (12) is

$$\begin{bmatrix} F_o(\underline{k}) \\ F_{\omega}(\underline{k}) \end{bmatrix} = \frac{1}{16 - m_c^2} \begin{bmatrix} 4 & -m_c \\ -m_c & 4 \end{bmatrix} \times \begin{bmatrix} 1 & 1 & 1 & 1 \\ e^{i2\pi k_x \Delta} & e^{-i2\pi k_x \Delta} & e^{i2\pi k_y \Delta} & e^{-i2\pi k_y \Delta} \end{bmatrix} \times \begin{bmatrix} S_{+x}(\underline{k}) \\ S_{-x}(\underline{k}) \\ S_{+y}(\underline{k}) \\ S_{-y}(\underline{k}) \end{bmatrix}. \quad (20)$$

One important observation is that $(\mathbf{H}^\dagger \mathbf{H})^{-1}$ is singular at k -space points for which $|m_p| = 2$ or $|m_c| = 4$. In general, a solution to (17) does not exist at $k_\rho = n_\rho \pi / \Delta$ where n_ρ is an integer. Similarly, a solution to (20) does not exist at: $(k_x, k_y) = ((2\pi n_x / \Delta), (2\pi n_y / \Delta))$ or $(k_x, k_y) = ((\pi / \Delta) + (2\pi n_x / \Delta), (\pi / \Delta) + (2\pi n_y / \Delta))$, where n_x and n_y are arbitrary integers. However, Δ is a parameter that can be varied experimentally and, thus, we can control the occurrences of singularities in a finite region of k -space.

III. MATERIALS AND METHODS

To demonstrate the technique, simulations and imaging experiments using phantoms and human volunteers were carried out.

A. Computer Simulations

Computer-simulated data were used to evaluate the effect of the choice of Δ on image quality (see Figs. 5 and 6 in Section V). Cartesian and radial k -space data of an object consisting of an outer circle containing four small circles were generated analytically [51]. A linear phase was added to the analytical expression of the k -space data of the shifted objects to produce the desired spatial shift. The matrix size of the discrete k -space data was 256×256 . Random uncorrelated gaussian noise was added to the k -space data to yield a signal-to-noise ratio (SNR) of 15 in the images after Fourier transformation. All programming was performed using the IDL software package (Research Systems, Inc., Boulder, CO)

B. MRI Experiments

A water/oil phantom was made by placing four 2-cm-diameter vials, two containing water and two containing mineral oil, in a 7-cm-diameter container filled with water. *In vivo* experiments were carried out on human volunteers.

MRI data were acquired on a GE Signa 1.5 T scanner (Milwaukee, WI) equipped with actively shielded gradients. The radial k -space data were acquired with a spin-echo pulse sequence modified to acquire k -space data along radial lines [52]. Data were generated by acquiring two sets of k -space data with opposite polarities of the readout gradients. The four sets of Cartesian k -space data were acquired with a conventional spin-echo MRI pulse sequence using four directions of the readout gradient $(x, -x, y, -y)$, respectively. In all cases, the data matrix was 256×256 . The chemical shift difference between the species was measured from a single average MR spectrum acquired prior to data acquisition. This was done during the prescanning time and did not increase the total scan time. Data were acquired with water as the on-resonance species.

C. Data Processing

Data were transferred to a personal computer for processing according to the algorithms shown in (17) and (20). All programming was performed using IDL. Equations (17) and (20) assume an ideal system where the phase differences between measurements arise because of the read gradient orientation and the off-resonance condition. However, real MRI systems

have eddy currents that vary with the orientation of the read gradient, which results in additional phase differences between measurements. To overcome this problem in the radial data sets, a Fourier transformation was performed on each radial line to generate a set of projections and a magnitude operation was performed on each projection to eliminate phase variations between data sets due to eddy currents. The linear phase in k -space due to chemical shift results in a spatial shift in the projection domain and, therefore, it is not affected by the magnitude operation. An inverse Fourier transform of the magnitude projections was used to generate the complex data sets, $S_{+\rho}(\underline{k})$ and $S_{-\rho}(\underline{k})$, used in the algorithm. For Cartesian data, each data set was 2-D Fourier transformed to generate an image, then a magnitude operation was performed to eliminate phase differences between image data sets. The linear phase in k -space due to chemical shift results in a spatial shift in the image domain and, therefore, it is not affected by the magnitude operation. An inverse 2-D Fourier transform of the magnitude images was used to generate the complex data sets: $S_{+x}(\underline{k})$, $S_{-x}(\underline{k})$, $S_{+y}(\underline{k})$, and $S_{-y}(\underline{k})$. For *in vivo* data we checked for motion between data sets by comparing the position of an on-resonance structure in all images obtained from the measured data sets. In the data presented here, there was no misregistration among data sets due to motion.

In order to avoid computational problems, the central singularity in $(\mathbf{H}^\dagger \mathbf{H})^{-1}$ was set to the value of the nearest point. This value was then used as a threshold for all other data points in $(\mathbf{H}^\dagger \mathbf{H})^{-1}$. In some cases [Figs. 2(b)–(c) and 4(b)–(c)], the local spatial frequencies affected by the singularities in the high spatial frequency regions were further smoothed to reduce image artifacts. Smoothing was accomplished in a window of 11×11 k -space data points (centered at each singularity of $(\mathbf{H}^\dagger \mathbf{H})^{-1}$ in the high spatial frequency region of the measured k -space) by the bilinear interpolation of data points surrounding the region. Thus, 482 data points out of the 65536 k -space data points (0.74% of k -space) were smoothed.

In the calculations, the positional shift, Δ' , in pixels is used in lieu of the positional shift, Δ , in cm. The relationship between Δ' and Δ is given by

$$\Delta' = \frac{\gamma G_{\text{readout}} N_{\text{readout}}}{\text{BW}} \Delta \quad (21)$$

where BW is the receiver bandwidth and N_{readout} is the number of acquired data points in the readout direction. Since $\omega = \gamma G_{\text{readout}} \Delta$, Δ' is readily calculated from

$$\Delta' = \frac{\omega}{\text{BW}} N_{\text{readout}} \quad (22)$$

In the phantom experiments, we checked for the correct value of Δ' by varying its value in the algorithm to obtain the best separation of the two chemical shift images. The calculated and experimental values of Δ' agreed to ± 0.2 pixels. Based on these results, we used the calculated value of Δ' for the *in vivo* imaging experiments. Through all the experiments the number of acquisition points was kept constant ($N_{\text{readout}} = 256$) and Δ' was varied by changing the receiver bandwidth.

Images from Cartesian data were reconstructed using conventional 2-D Fourier transformation. Images from radial data were reconstructed using a complex filtered backprojection reconstruction algorithm [51].

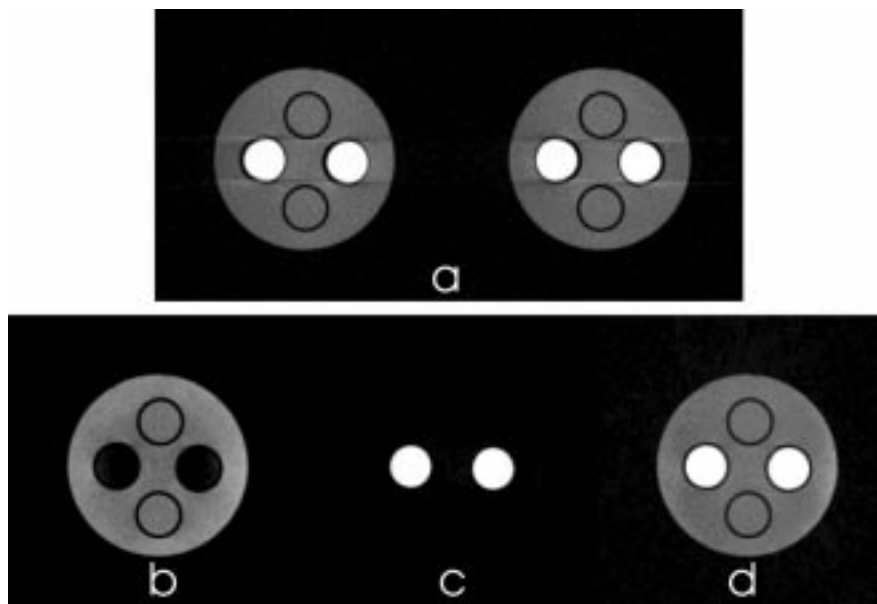


Fig. 1. (a) Images of a water/oil phantom obtained from radial data using two different directions of the readout gradient ($+\rho$ and $-\rho$) and a pixel shift, $\Delta' = 0.9$ pixels. Images were acquired with a radial spin-echo MRI pulse sequence with $TR/TE = 500$ ms/20 ms, number of signal averages, $NSA = 1$, $FOV = 12 \times 12$ cm², matrix size = 256×256 , $BW = \pm 31.3$ kHz, and slice thickness = 5 mm. The tuning-fork artifact at the edges of the two oil vials (the off-resonance species) is the typical chemical-shift artifact in data acquired with radial MRI. (b) Water and (c) lipid images obtained with algorithm (17) for the data set shown in (a). The images shown in (b) and (c) can be combined to generate a water and lipid image without the chemical-shift artifact, as shown in (d).

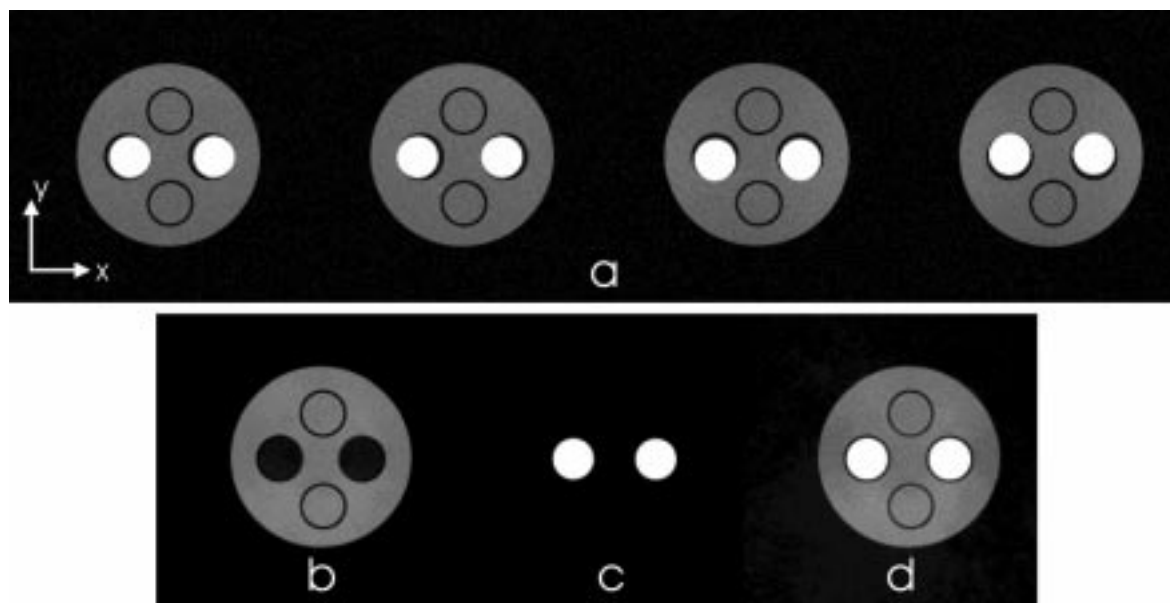


Fig. 2. (a) Images of a water/oil phantom obtained from Cartesian data using four different directions of the readout gradient (x , $-x$, y , and $-y$) and a pixel shift, $\Delta' = 1.8$ pixels. Images were acquired with a 2-D Fourier spin-echo MRI pulse sequence with $TR/TE = 500$ ms/20 ms, $NSA = 1$, $FOV = 12 \times 12$ cm², matrix size = 256×256 , $BW = \pm 16$ kHz, and slice thickness = 5 mm. The shift or misregistration of the position of the oil vials (the off-resonance species) along the direction of the readout gradient is the typical chemical-shift artifact. (b) Water and (c) lipid images obtained with algorithm (20) for the data set shown in (a). The images shown in (b) and (c) can be combined to generate a water and lipid image without the misregistration error, as shown in (d).

IV. RESULTS

Figs 1 and 2 show the results for the radial and Cartesian data, respectively, in a water/oil phantom. Fig. 1(a) shows the images of the water/oil phantom obtained from the two radial data sets: $S_{+\rho}(\underline{k})$ and $S_{-\rho}(\underline{k})$ acquired with $\Delta' = 0.9$ pixels. In these images, the chemical-shift artifact is a shift of the oil vials (i.e., the two bright circles in the central part of the phantom) and a “tuning-fork” artifact at the edges of the vials. This artifact is caused by the shift or misregistration of the position of

off-resonance species along each projection [53]. Fig. 1(b) and (c) shows the individual water and oil images obtained with algorithm (17). The images shown in Figs. 1(b) and (c) can be combined to generate a water and lipid image without the shift and tuning-fork artifact as shown in Fig. 1(d).

Fig. 2(a) shows the images of the water/oil phantom obtained by Fourier transformation of the four Cartesian data sets: $S_{+x}(\underline{k})$, $S_{-x}(\underline{k})$, $S_{+y}(\underline{k})$, and $S_{-y}(\underline{k})$ acquired with $\Delta' = 1.8$ pixels. In the four images, the chemical-shift arti-

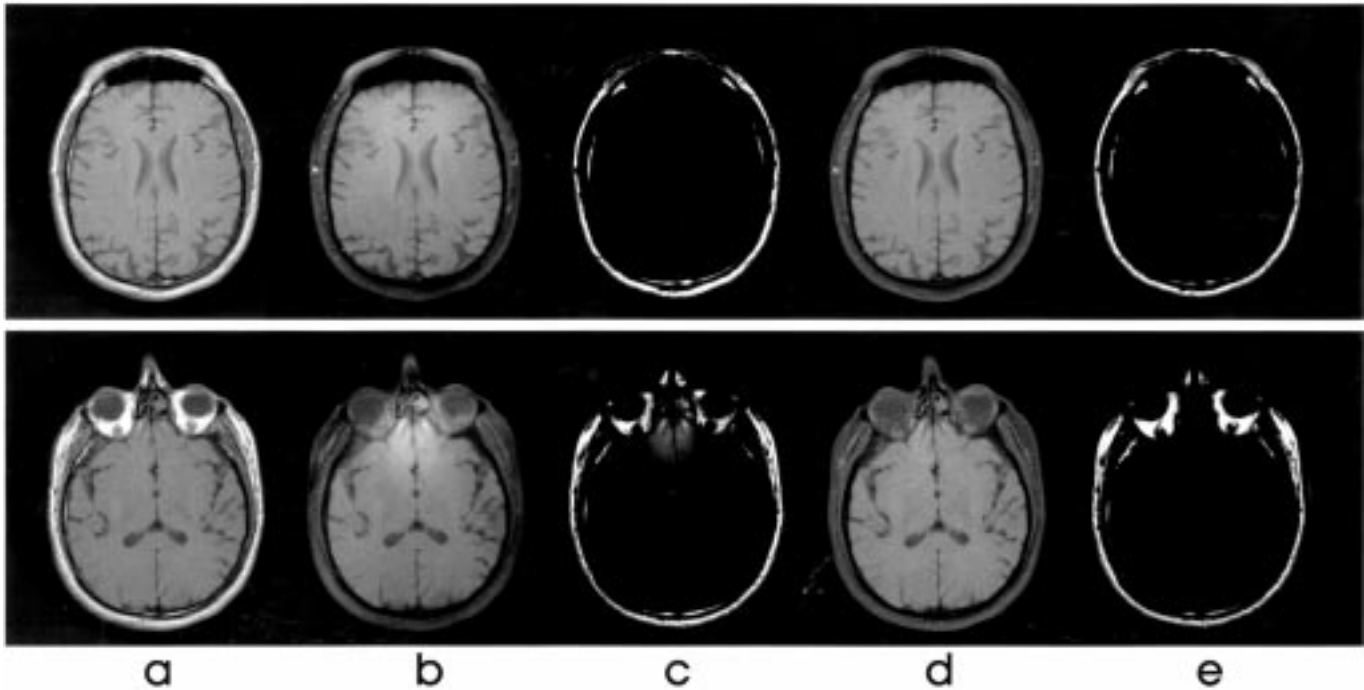


Fig. 3. (a) Images of two axial slices of a head acquired with a radial spin-echo MRI pulse sequence ($TR/TE = 800 \text{ ms}/20 \text{ ms}$, $NSA = 1$, $FOV = 24 \times 24 \text{ cm}^2$, matrix size = 256×256 , slice thickness = 5 mm , $BW = \pm 31.3 \text{ kHz}$). Data has contributions of both lipid and water. (b) Water and (c) lipid images obtained with algorithm (17) for $\Delta' = 0.9$ pixels. (d) Water and (e) lipid images obtained using a chemical-shift selective suppression pulse.

fact is clearly seen as a shift or misregistration of the position of the oil vials along the direction of the readout gradient. Fig. 2(b) and (c) shows the individual water and oil images obtained with algorithm (20). The two images can be combined to generate a water and lipid image without the misregistration error, as shown in Fig. 2(d). In both examples, the chemical-shift separation algorithms yielded a good separation between the two chemically shifted species. It should be pointed out that the value of Δ' used in the above examples was not chosen arbitrarily. Δ' was chosen to minimize artifacts caused by the singularities in $(\mathbf{H}^\dagger \mathbf{H})^{-1}$ as will be explained in Section V.

The chemical-shift separation method was also used to obtain water and lipid images *in vivo*. Results are shown in Figs. 3 and 4 for two axial head slices. The images shown in Fig. 3 were generated with radial data. The images shown in Fig. 4 were generated with Cartesian data. The images shown in Figs. 3(a) and 4(a) have both lipid and water contributions. The images shown in Figs. 3(b)–(c) and 4(b)–(c) are the individual water and lipid images obtained with algorithms (17) and (20), respectively. The images shown in Figs. 3(e)–(d) and 4(e)–(d) are the individual water and lipid images obtained with a conventional chemical-shift selective suppression method [6]. Although the chemical-shift separation method presented in this paper works fairly well in resolving the lipid and water components for the top slice shown in Figs. 3 and 4, the technique fails in regions where there is high tissue susceptibility. This is shown clearly in Figs. 3(b)–(c) and 4(b)–(c) for the bottom slice in regions close to the sinuses. There are also additional artifacts that are inherent to algorithms (17) and (20). These will be discussed in Section V.

V. DISCUSSION

From the examples shown above it is clear that the linear phase accumulated during the readout period due to chemical shift can be used to separate the contributions of chemically shifted species in an image. Although the algorithms will separate the two chemically shifted species at any Δ determined by (7), there are artifacts caused by the singularities in $(\mathbf{H}^\dagger \mathbf{H})^{-1}$ that depend on Δ . The functions $1/(4 - m_p^2)$ and $1/(16 - m_c^2)$ in $(\mathbf{H}^\dagger \mathbf{H})^{-1}$ amplify k -space data regions to correct for the attenuation in the operators $\begin{bmatrix} 2 & -m_p \\ -m_p & 2 \end{bmatrix} \begin{bmatrix} 1 & 1 \\ e^{i2\pi k_x \Delta} & e^{-i2\pi k_x \Delta} \end{bmatrix}$ and $\begin{bmatrix} 4 & -m_c \\ -m_c & 4 \end{bmatrix} \begin{bmatrix} 1 & 1 \\ e^{i2\pi k_x \Delta} & e^{-i2\pi k_x \Delta} \\ e^{i2\pi k_y \Delta} & e^{-i2\pi k_y \Delta} \end{bmatrix}$, respectively. In ideal noiseless data, there are no artifacts since the k -space regions attenuated by the above operators are amplified back to the correct value by the corresponding functions $1/(4 - m_p^2)$ and $1/(16 - m_c^2)$. This perfect attenuation and amplification procedure does not work when noise is present. Artifacts arise due to the boosting of noise components by the functions $1/(4 - m_p^2)$ and $1/(16 - m_c^2)$, thus, artifacts are accentuated in noisier data. The nature of the artifacts is shown in Figs. 5 and 6 for computer-simulated radial and Cartesian data, respectively. Fig. 5 shows the function $1/(4 - m_p^2)$ in the measured k -space region for various values of Δ' and the resultant images obtained from algorithm (17). Fig. 6 shows the function $1/(16 - m_c^2)$ in the measured k -space region for various values of Δ' and the resultant images obtained from algorithm (20). In both Figs. 5 and 6, we can identify two kinds of artifacts: 1) a slowly varying intensity across the image and 2) a grid pattern. The former is due to the amplification of the low-frequency noise near the center of k -space. This is more

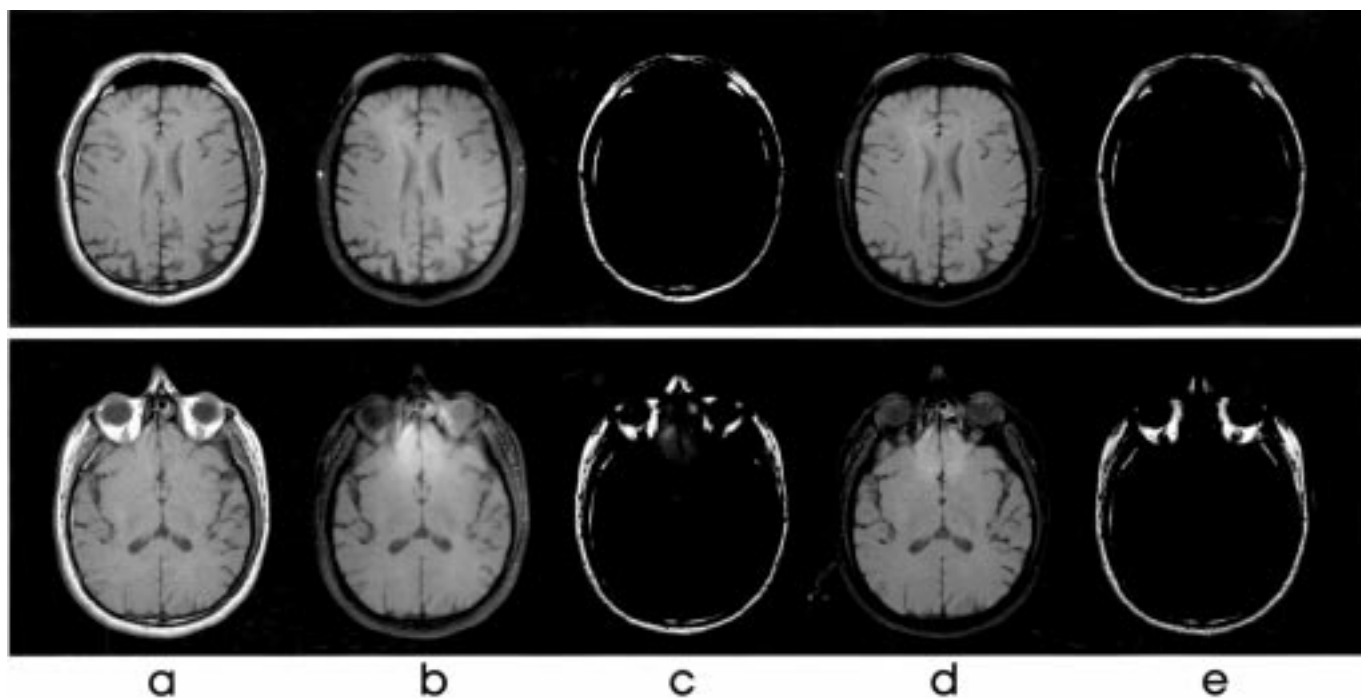


Fig. 4. (a) Images of two axial slices of a head acquired with a 2-D Fourier spin-echo MRI pulse sequence ($TR/TE = 800\text{ ms}/20\text{ ms}$, $NSA = 1$, $FOV = 24 \times 24\text{ cm}^2$, matrix size = 256×256 , slice thickness = 5 mm , $BW = \pm 16\text{ kHz}$). Data has contributions of both lipid and water. (b) Water and (c) lipid images obtained with algorithm (20) for $\Delta' = 1.8$ pixels. (d) Water and (e) lipid images obtained using a chemical-shift selective suppression pulse.

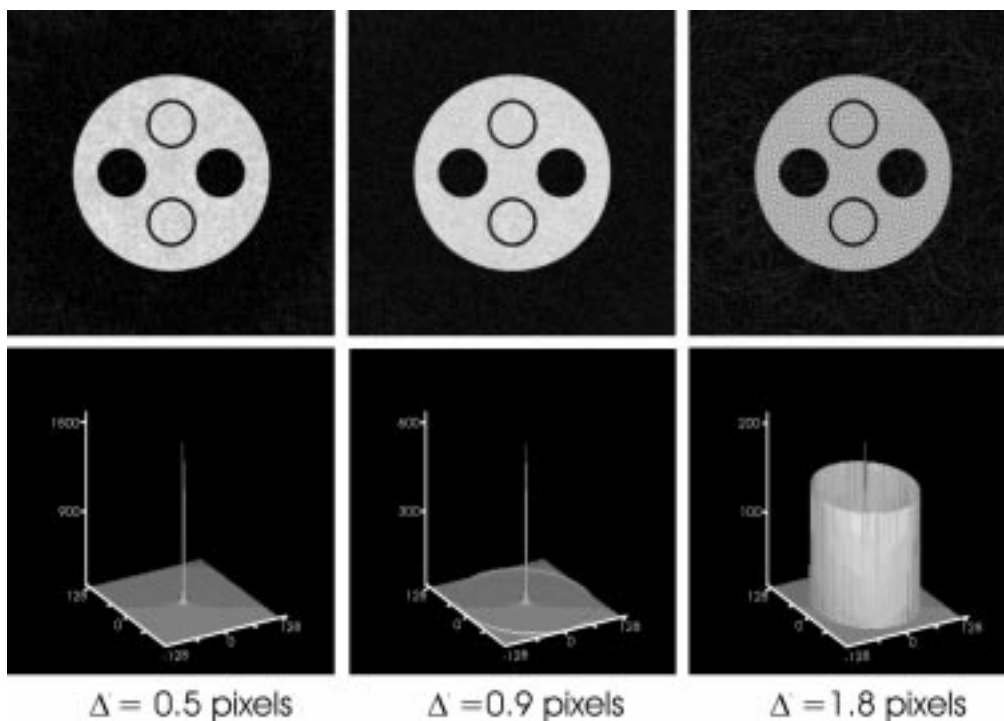


Fig. 5. Effect of the function $1/(4 - m_p^2)$ on image quality for various values of Δ' using computer generated data. (top) Images of the unshifted (i.e., on-resonance) species obtained with algorithm (17) followed filtered backprojection reconstruction. (bottom) Surface plots of the function $1/(4 - m_p^2)$.

pronounced at smaller values of Δ' because the height of the functions $1/(4 - m_p^2)$ and $1/(16 - m_c^2)$ in the low-frequency region is inversely proportional to Δ' . The grid pattern is attributable to the amplification of noise components in specific regions of k -space. The grid artifact is more pronounced as the number

of singularities in a measured region of k -space increases, i.e., at higher values of Δ' . For Cartesian data (Fig. 6), a good compromise between these competing conditions is to choose Δ' in the range of 0.9 to 1.8 pixels. At $\Delta' = 0.9$ pixels there is only one singularity at the center of k -space. At $\Delta' = 1.8$ pixels there are

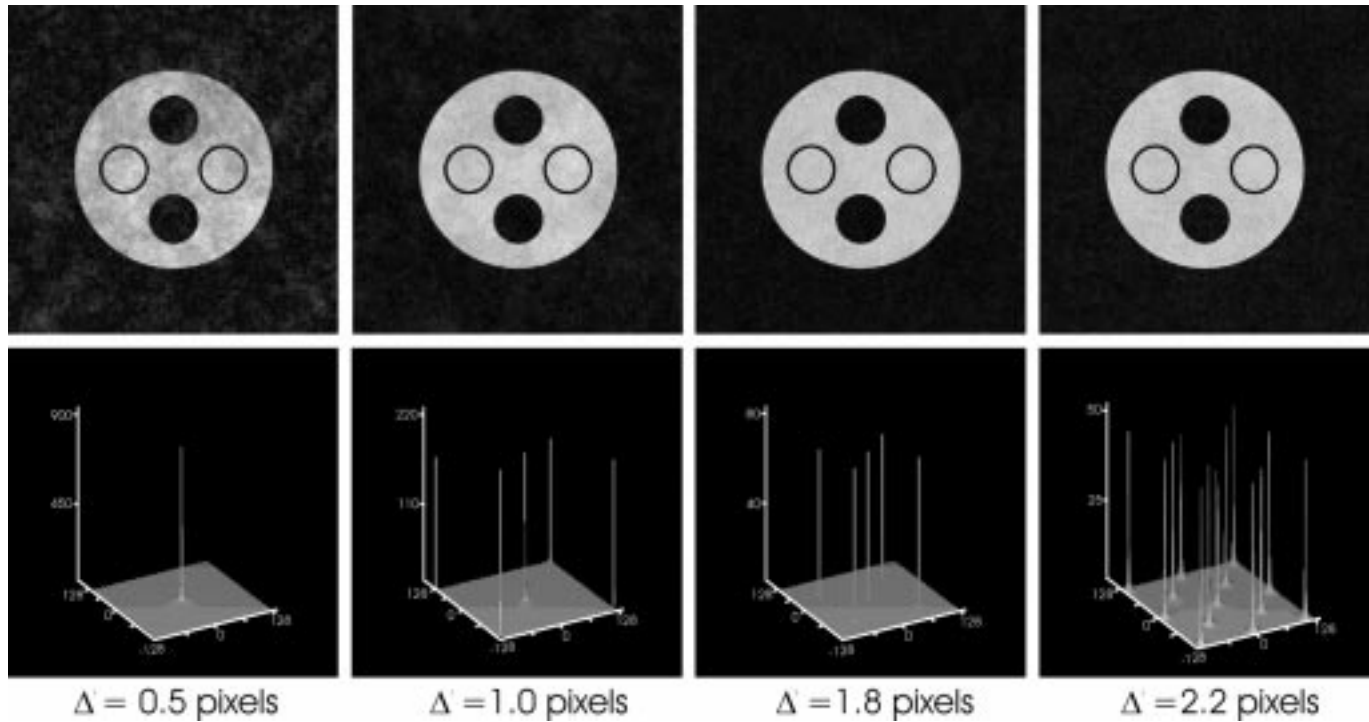


Fig. 6. Effect of the function $1/(16 - m_c^2)$ on image quality for various values of Δ' using computer generated data. (top) Images of the unshifted (i.e., on-resonance) species obtained with algorithm (20) followed by 2-D Fourier transformation. (bottom) Surface plots of the function $1/(16 - m_c^2)$.

four maxima¹ of the function $1/(16 - m_c^2)$ in the high-spatial frequency region. The grid artifact can be reduced by smoothing the data in those regions. Nevertheless, the grid artifact is always present to some extent and is more evident in noisier data. In the images shown in Figs. 2(b)–(c) and 4(b)–(c), smoothing was performed, however, the grid artifact is still apparent in Fig. 4(b) around the eyes in the bottom slice. In the radial case (Fig. 5), the function $1/(4 - m_p^2)$ affects every k -space point at a radius π/Δ' , thus, for $\Delta' > 1$ the grid artifact is quite significant even after smoothing. Thus, for the radial case a good choice of Δ' is 0.9 pixels. The chemical-shift separation for water and fat on a typical 1.5 T clinical MRI scanner is 220 Hz. Δ' values of 1.8 and 0.9 pixels are easily achieved using imaging parameters such as $N_{\text{readout}} = 256$ points and BW values of ± 16 and ± 32 KHz, respectively [see (22)]. If a different bandwidth is desired, N_{readout} has to be adjusted according to (22).

The SNR is another parameter that is dependent on Δ' . To derive an expression for the SNR we can rewrite (17) and (20) as follows:

$$\begin{bmatrix} F_o(\underline{k}) \\ F_w(\underline{k}) \end{bmatrix} = \begin{bmatrix} \varepsilon_{00}^p & \varepsilon_{01}^p \\ \varepsilon_{10}^p & \varepsilon_{11}^p \end{bmatrix} \begin{bmatrix} S_{+\rho}(\underline{k}) \\ S_{-\rho}(\underline{k}) \end{bmatrix} \quad (23)$$

$$\begin{bmatrix} F_o(\underline{k}) \\ F_w(\underline{k}) \end{bmatrix} = \begin{bmatrix} \varepsilon_{00}^c & \varepsilon_{01}^c & \varepsilon_{02}^c & \varepsilon_{03}^c \\ \varepsilon_{10}^c & \varepsilon_{11}^c & \varepsilon_{12}^c & \varepsilon_{13}^c \end{bmatrix} \begin{bmatrix} S_{+x}(\underline{k}) \\ S_{-x}(\underline{k}) \\ S_{+y}(\underline{k}) \\ S_{-y}(\underline{k}) \end{bmatrix}. \quad (24)$$

Since the coefficients ε are dependent on \underline{k} , the SNR of data processed with algorithms (17) and (20) is also dependent on \underline{k} (i.e., the noise is no longer white and the SNR is object-dependent). To calculate the SNR we assume a point object so that

¹For a discrete k -space region, singularities may not fall at specific measurement points (except for $\underline{k} = 0$ which is always singular). Thus, we use the term maxima instead of singularity.

the energy in k -space is evenly distributed over all spatial frequencies. In this case, k -space measurements are independently identically distributed (iid) random variables with mean, \bar{S} (\bar{S} contains all the parameters associated with the measurement of the data), and variance, α_k . We then sum the signal and the variance of the noise over all spatial frequencies. For radial data, the SNR for the image of one of the species (i.e., the on-resonance species) can be calculated from

$$\text{SNR}^P = \sqrt{N_\theta} \frac{\bar{S}}{\sigma_k} \frac{\sum_{k_\rho} \sum_{i=0}^1 \text{filter}(k_\rho) \varepsilon_{01}^p(k_\rho)}{\sqrt{\sum_{k_\rho} \sum_{i=0}^1 |\text{filter}(k_\rho) \varepsilon_{01}^p(k_\rho)|^2}} \quad (25)$$

where $\text{filter}(k_\rho)$ is the ramp function used in filtered backprojection to compensate for the oversampling of the low frequencies in k -space [51], and N_θ is the number of radial lines acquired. To compare SNR^P to the SNR of an image obtained from $S_{+\rho}(\underline{k})$ or $S_{-\rho}(\underline{k})$ after filtered backprojection reconstruction, a reference value can be computed

$$\text{SNR}_{\text{ref}}^P = \sqrt{N_\theta} \frac{\bar{S}}{\sigma_k} \frac{\sum_{k_\rho} \sum_{i=0}^1 \text{filter}(k_\rho)}{\sqrt{\sum_{k_\rho} \sum_{i=0}^1 |\text{filter}(k_\rho)|^2}}. \quad (26)$$

For Cartesian data, the SNR for the image of one species (the on-resonance species) is

$$\text{SNR}^C = \frac{\bar{S}}{\sigma_k} \frac{\sum_{k_x} \sum_{k_y} \sum_{i=0}^3 \varepsilon_{0i}^c(\underline{k})}{\sqrt{\sum_{k_x} \sum_{k_y} \sum_{i=0}^3 |\varepsilon_{0i}^c(\underline{k})|^2}}. \quad (27)$$

The SNR of one image obtained from either $S_{+x}(\underline{k})$, $S_{-x}(\underline{k})$, $S_{+y}(\underline{k})$, or $S_{-y}(\underline{k})$ is

$$\text{SNR}_{\text{ref}}^C = \frac{\bar{S}}{\sigma_k} \sqrt{N_{k_x} N_{k_y}} \quad (28)$$

where N_{k_x} and N_{k_y} are the number of k_x and k_y data points, respectively.

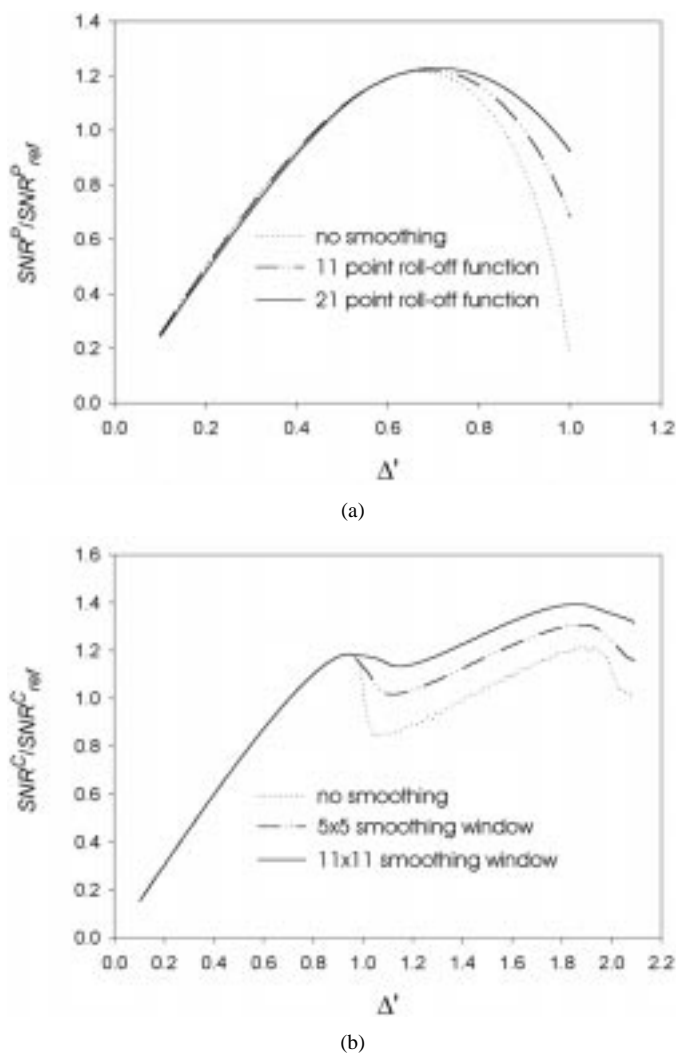


Fig. 7. Dependence of the SNR with Δ' . (a) $\text{SNR}^P/\text{SNR}_{\text{ref}}^P$ for the images obtained with algorithm (17). For $\Delta' > 0.6$, $\text{SNR}^P/\text{SNR}_{\text{ref}}^P$ can be improved by rolling-off the data points near the edges of the measured k -space. Roll-off was accomplished by using a linear ramp to zero after the cutoff point, which was positioned at 11 or 21 data points from the edges of the measured k -space. (b) $\text{SNR}^C/\text{SNR}_{\text{ref}}^C$ for the images obtained with algorithm (20). For $\Delta' > 0.9$, $\text{SNR}^C/\text{SNR}_{\text{ref}}^C$ can be improved by smoothing the local spatial frequencies affected by the singularities in the high-spatial frequency region. Smoothing was accomplished in a region of 5×5 or 11×11 k -space data points centered at the singularities by the bilinear interpolation of data points surrounding the region.

The dependence of $\text{SNR}^P/\text{SNR}_{\text{ref}}^P$ and $\text{SNR}^C/\text{SNR}_{\text{ref}}^C$ with Δ' is shown in Fig. 7. Again, we have the two competing situations: as Δ' increases the height of the functions $1/(4 - m_p^2)$ and $1/(16 - m_c^2)$ near the central singularity decreases and this has the effect of increasing the SNR. However, as Δ' increases there are more maxima of the functions $1/(4 - m_p^2)$ and $1/(16 - m_c^2)$ that enter the measured region of k -space and this decreases the SNR. For $\text{SNR}^P/\text{SNR}_{\text{ref}}^P$, there is a maximum around $\Delta' = 0.6$ – 0.7 pixels. As shown in Fig. 7(a), $\text{SNR}^P/\text{SNR}_{\text{ref}}^P$ can be improved for higher values of Δ' by rolling-off the values of the function $1/(4 - m_p^2)$ near the edges of the measured k -space. For $\text{SNR}^C/\text{SNR}_{\text{ref}}^C$, there is a maximum around $\Delta' = 0.9$ pixels [see Fig. 7(b)]. If local smoothing is applied around the singular points in the high-spatial frequency regions of the measured k -space, the SNR for higher values of Δ' can be im-

proved. Depending on the amount of smoothing, the maximum $\text{SNR}^C/\text{SNR}_{\text{ref}}^C$ can be shifted from $\Delta' = 0.9$ pixels to $\Delta' = 1.8$ – 1.9 pixels.

There are advantages of the chemical-shift separation method for radial data over Cartesian data. The major advantage is that only two sets of data are needed rather than four, so the experiment can be done in half the time. One could develop an algorithm for the Cartesian case using only two data sets, but it would result in singularities along k -space lines. For any value of Δ' , there will be a singular line passing through $\underline{k} = 0$ and this will produce horizontal or vertical stripes in the image depending on the direction of the readout gradient. This was the problem with a similar chemical-shift separation method developed by Axel *et al.* for Cartesian data using only two data sets [48]. In the radial case, there is only a singularity at the center point of k -space, so it is not necessary to acquire more than two data sets. We can compare the imaging efficiency of the two methods using a quantity called “noise performance” defined as the ratio of the SNR obtained for each chemically shifted species relative to the SNR expected for the number of signal averages (NSA) in a conventional scan. For the radial case, $\text{SNR}^P/\text{SNR}_{\text{ref}}^P = 1.22$ compared with $\text{SNR} = \sqrt{2}$ obtained for a conventional NSA = 2. For the Cartesian case, $\text{SNR}^C/\text{SNR}_{\text{ref}}^C = 1.3$ – 1.4 compared with an $\text{SNR} = 2$ for a conventional NSA = 4. Thus, the noise performance of the radial method is 0.86 and for the Cartesian method is 0.7.

The chemical-shift separation method described here has the drawback of being sensitive to magnetic-field inhomogeneities and tissue susceptibilities. As shown in Figs. 3 and 4, the method fails to give the correct separation of the species in the presence of field inhomogeneities because the resonant frequencies and resulting positional shifts are spatially variant. The method can be modified to correct for field inhomogeneities provided that the static field map distribution is known. Data for calculating the field map can be obtained by adding a second readout period before or after the readout of the data required for algorithms (17) and (20). These additional data have to be acquired with the same readout gradient orientation but with a different spin-echo point in order to generate the constant phase differences needed for the field map [24]. The increase of the total experimental time for acquiring data with a field map will be minimal. A general description of a correction scheme is given in the Appendix.

The most widely used chemical-shift method is where one species is eliminated by an adequate suppression scheme (i.e., chemical-shift selective excitation, inversion recovery, or diffusion). With chemical-shift suppression methods, a minimum of two acquisitions are required to obtain images of two chemically shifted species. Each one will have a maximum of $\text{SNR}/\text{SNR}_{\text{ref}} = 1.0$, although the signal intensity can be worse because of partial suppression of the desired signal due to the bandwidth of the selective radio-frequency pulse, partial recovery during the inversion time, or diffusion of the species. With four acquisitions, each chemically shifted image will have a maximum $\text{SNR}/\text{SNR}_{\text{ref}} = \sqrt{2}$. The noise performance obtained with techniques that use a chemical-shift suppression pulse is 0.7. Thus, our Cartesian method has a comparable noise performance to chemical-shift suppression methods. The

radial method has a higher noise performance (i.e., 0.86) than chemical-shift suppression methods. However, our SNR calculations were for a point object. The actual noise performance may be different for real objects that have more energy at the lower spatial frequencies. Indeed, the measured SNR for the head data shown in Figs. 3 and 4 was 15%–20% less than the calculated values. Chemical-shift suppression methods are also sensitive to magnetic-field inhomogeneities and tissue susceptibilities (if a chemical-shift selective pulse is used), or tissue T1-dispersion (if an inversion-recovery method is used). The results shown in Figs. 3 and 4 indicate that the sensitivity to magnetic-field inhomogeneities and tissue susceptibilities of methods that use a chemical-shift selective pulse is less than for our technique. However, the correction scheme described in the Appendix may improve this situation.

The three-point Dixon method is an alternative chemical-shift method that is less sensitive to magnetic-field inhomogeneities and tissue susceptibilities. In the three-point Dixon method, a map of the magnetic field is calculated from the data acquired for the clinical images and is used to correct for magnetic-field inhomogeneities and tissue susceptibilities to a certain extent [24], [25]. The noise performance of the Dixon method is reported to be 0.95 [24] which is higher than the chemical-shift method presented here as well as other chemical-shift selective methods. A careful comparison between our technique and the Dixon method will need to be performed once our method is modified to correct for magnetic-field inhomogeneities and tissue susceptibilities. A potential advantage of the radial method presented here is that the two data sets can be acquired back-to-back in one acquisition. This approach has been tested with Dixon to reduce the total acquisition time [21], [23], [29], [31], [32], however, the acquisition timing of the data sets is quite different (~ 20 ms) and this can introduce artifacts in the resulting images. In the radial method, only a gradient reversal is needed to obtain the two data sets and this could be done in a short time (< 4 ms). A potential problem with the chemical-shift method developed here (as well as with the Dixon method) is misregistration of position between data sets due to patient motion. This problem can be corrected by comparing the position of an on-resonance structure in all images obtained from the initial data sets and shifting the images, or adding a linear phase to the k -space data, such that the on-resonance structure in all images has the same position.

The chemical-shift separation method described here can be extended to more than two species, provided that the number of acquired data sets is equal to or greater than the number of species. Potentially, up to four species can be resolved with the four data sets required for the Cartesian method. The chemical-shift separation method can also be used in combination with other methods to separate more than two species or to improve the separability of a single species.

VI. CONCLUSION

A technique is described that separates contributions in an image from different chemically shifted species based on the linear phase in k -space acquired during the readout period. The technique was demonstrated for two chemically shifted species

and for radial and Cartesian data. We show that the choice of Δ , which is the positional shift due to off-resonance along the readout direction in image space, is important in determining image quality (i.e., image artifacts and SNR). The technique is sensitive to magnetic-field inhomogeneities and tissue susceptibilities. A general method for correcting the distortions in the data induced by magnetic-field inhomogeneities and tissue susceptibilities is presented in the Appendix. The chemical-shift separation method developed for radial data has a time advantage and a higher noise performance compared with the Cartesian method. While the method was demonstrated for two chemically shifted species, it can be extended to more components.

APPENDIX

Magnetic-field inhomogeneities or tissue susceptibilities produce geometric distortions in the object. These distortions change with the different orientations of the readout gradient and cause errors for the chemical-shift method presented herein. If these distortions can be removed, we can apply algorithms (17) and (20) to obtain chemical-shift images without the effects of magnetic-field inhomogeneities or tissue susceptibilities. We show a general approach for distortion correction for the Cartesian case but a similar method can be derived for the radial case as well. The approach assumes that we have prior knowledge of a field map, $\Delta B(x, y)$. For a vector $\underline{r} = \begin{bmatrix} x \\ y \end{bmatrix}$, a distortion operator can be expressed by

$$\hat{D}(\underline{r}) = \begin{bmatrix} x + a_n u(x, y) \\ y + b_n u(x, y) \end{bmatrix} \quad (29)$$

where a_n and b_n indicate the relative orientations of the readout gradient on each acquisition and $u(x, y)$ is the spatial shift induced by the inhomogeneities or tissue susceptibilities [i.e., $u(x, y) \propto \Delta B(x, y)$]. For the four acquisitions used in the Cartesian case, the values of a_n and b_n are

n	a_n	b_n
1	1	0
2	-1	0
3	0	1
4	0	-1

The equation for the signal intensity in the space domain for two chemically shifted species, considering both chemical shift and the distortions due to inhomogeneities and tissue susceptibilities, is

$$I_n(\underline{r}) = m_o(\hat{D}_n(\underline{r})) + m_\omega(\hat{D}_n(\underline{r}) + \underline{\Delta}_n) \quad (30)$$

where m_o and m_ω are the contributions from the on-resonance and off-resonance species, respectively, and $\underline{\Delta}_n = \begin{bmatrix} a_n \\ b_n \end{bmatrix} \Delta$. The distortion operator, $\hat{D}_n(\underline{r})$, can be removed from (30) by calculating its inverse

$$I_n(\hat{D}_n^{-1}(\underline{r})) = m_o(\underline{r}) + m_\omega(\underline{r} + \underline{\Delta}_n). \quad (31)$$

The corrected images can then be used with algorithms (17) and (20) after Fourier transformation. If we assume a smoothly varying field map, then $\hat{D}_n^{-1}(\underline{r})$ exists in a continuous domain. Since both the data and $u(x, y)$ are discrete, the inverse has to be obtained by the appropriate interpolation.

REFERENCES

- [1] M. Komiyama, T. Yasui, H. Yagura, Y. Fu, H. Sugata, M. Kiyama, and M. Baba, "Chemical-shift misregistration effect in spinal magnetic resonance imaging," *Neurologia Medico-Chirurgica*, vol. 28, pp. 642–644, 1988.
- [2] A. S. Smith, M. A. Weinstein, G. C. Hurst, D. R. DeRemer, R. A. Cole, and P. M. Duchesneau, "Intracranial chemical-shift artifacts on MR images of the brain: Observations and relation to sampling bandwidth," *Amer. J. Roent.*, vol. 154, pp. 1275–1283, 1990.
- [3] P. M. Parizel, B. A. van Hasselt, L. van den Hauwe, J. W. Van Goethem, and A. M. De Schepper, "Understanding chemical shift induced boundary artefacts as a function of field strength: Influence of imaging parameters (bandwidth, field-of-view, and matrix size)," *European J. Radiol.*, vol. 18, pp. 158–164, 1994.
- [4] R. W. Whitehouse, C. E. Hutchinson, R. Laitt, J. P. Jenkins, and A. Jackson, "The influence of chemical shift artifact on magnetic resonance imaging of the ligamentum flavum at 0.5 tesla," *Spine*, vol. 22, pp. 200–202, 1997.
- [5] B. R. Rosen, V. J. Wedeen, and T. J. Brady, "Selective saturation NMR imaging," *J. Comput. Assist. Tomogr.*, vol. 8, pp. 813–818, 1984.
- [6] A. Haase, J. Frahm, W. Haenicke, and D. Matthaei, "¹H NMR chemical-shift selective (CHESS) imaging," *Phys. Med. Biol.*, vol. 30, pp. 341–344, 1985.
- [7] P. M. Joseph and A. Shetty, "A comparison of selective saturation and selective echo chemical-shift imaging techniques," *Magn. Reson. Imag.*, vol. 6, pp. 421–430, 1988.
- [8] C. H. Meyer, J. M. Pauly, A. Macovski, and D. G. Nishimura, "Simultaneous spatial and spectral selective excitation," *Magn. Reson. Med.*, vol. 15, pp. 287–304, 1990.
- [9] J. Mao, H. Yan, and W. D. Bidgood Jr., "Fat suppression with an improved selective presaturation pulse," *Magn. Reson. Imag.*, vol. 10, pp. 49–53, 1992.
- [10] G. M. Bydder and I. R. Young, "MR imaging: Clinical use of the inversion recovery sequence," *J. Comput. Assist. Tomogr.*, vol. 9, pp. 659–675, 1985.
- [11] S. W. Atlas, R. I. Grossman, D. B. Hackney, H. I. Goldberg, L. T. Bilaniuk, and R. A. Zimmerman, "STIR MR imaging of the orbit," *AJR*, vol. 151, pp. 1025–1030, 1988.
- [12] L. L. Baker, S. B. Goodman, I. Perkash, B. Lane, and D. R. Enzmann, "Benign versus pathologic compression fractures of vertebral bodies: Assessment with conventional spin-echo, chemical-shift, and STIR MR imaging," *Radiology*, vol. 174, pp. 495–502, 1990.
- [13] C. J. Bakker, T. D. Witkamp, and W. M. Janssen, "Short TI short TR inversion recovery imaging using reduced flip angles," *Magn. Reson. Imag.*, vol. 9, pp. 323–330, 1991.
- [14] P. C. M. van Zijl and C. T. Moonen, "Complete water suppression for solutions of large molecules based on diffusional differences between solute and solvent (DRYCLEAN)," *J. Magn. Reson.*, vol. 87, pp. 18–25, 1990.
- [15] M. I. Altbach, M. A. Mattingly, M. F. Brown, and A. F. Gmitro, "Magnetic resonance imaging of lipid deposits in human atheroma via a stimulated-echo diffusion-weighted technique," *Magn. Reson. Med.*, vol. 20, pp. 319–261, 1991.
- [16] E. Kaldoudi, S. C. Williams, G. J. Barker, and P. S. Tofts, "A chemical-shift selective inversion recovery sequence for fat-suppressed MRI: Theory and experimental validation," *Magn. Reson. Imag.*, vol. 11, pp. 341–355, 1993.
- [17] M. I. Altbach, T. P. Trouard, R. J. Theilmann, G. C. Hunter, and A. F. Gmitro, "Detection of atherosclerotic lipids in *ex-vivo* tissue at 1.5 T," in *Proc. ISMRM, 4th Annu. Meeting*, New York, 1996, p. 723.
- [18] —, "A diffusion-weighted projection reconstruction method for detecting atherosclerotic lipids at 1.5 tesla," in *Proc. ISMRM, 5th Annu. Meeting*, Vancouver, BC, 1997, p. 794.
- [19] W. T. Dixon, "Simple proton spectroscopic imaging," *Radiology*, vol. 153, pp. 189–194, 1984.
- [20] R. E. Sepponen, J. T. Sipponen, and J. I. Tanttu, "A method for chemical-shift imaging: Demonstration of bone marrow involvement with proton chemical-shift imaging," *J. Comput. Assist. Tomogr.*, vol. 8, pp. 585–587, 1984.
- [21] H. N. Yeung, D. W. Kormos, and D. A. Sebok, "Single-acquisition chemical-shift imaging of a binary system with use of stimulated echoes," *Radiology*, vol. 167, pp. 537–540, 1988.
- [22] G. Brix, L. R. Schad, and W. J. Lorenz, "¹H-spectroscopic imaging using a modified Dixon method," *Magn. Reson. Imag.*, vol. 6, pp. 617–622, 1988.
- [23] S. C. Williams, M. A. Horsfield, and L. D. Hall, "True water and fat MR imaging with use of multiple-echo acquisition," *Radiology*, vol. 173, pp. 249–253, 1989.
- [24] G. H. Glover and E. Schneider, "Three-point Dixon technique for true water/fat decomposition with B0 inhomogeneity correction," *Magn. Reson. Med.*, vol. 18, pp. 371–383, 1991.
- [25] G. H. Glover, "Multipoint Dixon technique for water and fat proton and susceptibility imaging," *J. Magn. Reson. Imag.*, vol. 1, pp. 521–530, 1991.
- [26] T. W. Chan, J. Listerud, and H. Y. Kressel, "Combined chemical-shift and phase-selective imaging for fat suppression: Theory and initial clinical experience," *Radiology*, vol. 181, pp. 41–47, 1991.
- [27] J. Szumowski, W. R. Coshov, F. Li, and S. F. Quinn, "Phase unwrapping in the three-point Dixon method for fat suppression MR imaging," *Radiology*, vol. 192, pp. 555–561, 1994.
- [28] P. A. Hardy, R. S. Hinks, and J. A. Tkach, "Separation of fat and water in fast spin-echo MR imaging with the three-point Dixon technique," *J. Magn. Reson. Imag.*, vol. 5, pp. 181–185, 1995.
- [29] J. Szumowski, W. Coshov, F. Li, B. Coombs, and S. F. Quinn, "Double-echo three-point-Dixon method for fat suppression MRI," *Magn. Reson. Med.*, vol. 34, pp. 120–124, 1995.
- [30] B. D. Coombs, J. Szumowski, and W. Coshov, "Two-point Dixon technique for water-fat signal decomposition with B0 inhomogeneity correction," *Magn. Reson. Med.*, vol. 38, pp. 884–889, 1997.
- [31] F. Lethimonnier, F. Franconi, and S. Akoka, "Three-point Dixon method with a MISSTEC sequence," *Magma*, vol. 5, pp. 285–288, 1997.
- [32] J. Ma, F. W. Wehrli, H. K. Song, and S. N. H. Wang, "A single-scan imaging technique for measurement of the relative concentrations of fat and water protons and their transverse relaxation times," *J. Magn. Reson.*, vol. 125, pp. 92–101, 1997.
- [33] T. E. Skinner and G. H. Glover, "An extended two-point Dixon algorithm for calculating separate water, fat, and B0 images," *Magn. Reson. Med.*, vol. 37, pp. 628–630, 1997.
- [34] Q. S. Xiang and L. An, "Water-fat imaging with direct phase encoding," *J. Magn. Reson. Imag.*, vol. 7, pp. 1002–1015, 1997.
- [35] Y. Wang, D. Li, E. M. Haacke, and J. J. Brown, "A three-point Dixon method for water and fat separation using 2D and 3D gradient-echo techniques," *J. Magn. Reson. Imag.*, vol. 8, pp. 703–710, 1998.
- [36] T. R. Brown, B. M. Kincaid, and K. Ugurbil, "NMR chemical-shift imaging in three dimensions," in *Proc. Nat. Acad. Sci.*, vol. 79, USA, 1982, pp. 3523–3526.
- [37] A. A. Maudsley and S. K. Hilal, "Spatially resolved high resolution spectroscopy by four dimensional NMR," *J. Magn. Reson.*, vol. 51, pp. 147–152, 1983.
- [38] J. H. Duijn, G. B. Matson, A. A. Maudsley, and M. W. Weiner, "3D phase encoding 1H spectroscopic imaging of human brain," *Magn. Reson. Imag.*, vol. 10, pp. 315–319, 1992.
- [39] C. T. W. Moonen, G. Sobering, P. C. M. van Zijl, J. Gillen, M. von Kienlin, and A. Bizzi, "Proton spectroscopic imaging of human brain," *J. Magn. Reson.*, vol. 98, pp. 556–575, 1992.
- [40] J. R. Alger, S. C. Symko, A. Bizzi, S. Posse, D. J. DesPres, and M. R. Armstrong, "Absolute quantitation of short TE brain 1H MR spectra and spectroscopic imaging data," *J. Comput. Assist. Tomogr.*, vol. 17, pp. 191–199, 1993.
- [41] J. H. Duy and C. T. W. Moonen, "Fast proton spectroscopic imaging of human brain using multiple spin echoes," *Magn. Reson. Med.*, vol. 30, pp. 409–414, 1993.
- [42] O. Gonen, F. Arias-Mendoza, and G. Goelman, "3D Localized *in vivo* ¹H spectroscopy of human brain by using a hybrid of 1D-Hadamard with 2D-chemical-shift imaging," *Magn. Reson. Med.*, vol. 37, pp. 644–650, 1997.
- [43] P. Mansfield, "Spatial mapping of the chemical shift in NMR," *Magn. Reson. Med.*, vol. 1, pp. 370–386, 1984.
- [44] A. Macovski, "Volumetric NMR imaging with time-varying gradients," *Magn. Reson. Med.*, vol. 2, pp. 29–40, 1985.
- [45] D. N. Guilfoyle, A. Blamire, B. Chapman, R. J. Ordidge, and P. Mansfield, "PEEP—a rapid chemical-shift imaging method," *Magn. Reson. Med.*, vol. 10, pp. 282–287, 1989.
- [46] D. B. Tweig, "Multiple-output chemical shift imaging (MOCSI): A practical technique for rapid spectroscopic imaging," *Magn. Reson. Med.*, vol. 12, pp. 64–73, 1989.
- [47] S. Posse, T. Giocchino, R. Risinger, R. Ogg, and D. L. Bihan, "High-speed 1H spectroscopic imaging in the human brain by echo-planar spatial-spectral encoding," *Magn. Reson. Med.*, vol. 33, pp. 34–40, 1995.
- [48] E. Adalsteinsson, P. Irarrazabal, S. Topp, C. Meyer, A. Macovski, and D. M. Spielman, "Volumetric spectroscopic imaging with spiral-based *k*-space trajectories," *Magn. Reson. Med.*, vol. 39, pp. 889–898, 1998.

- [49] L. Axel, G. H. Glover, and N. Pelc, "Chemical-shift magnetic resonance imaging of two-line spectra by gradient reversal," *Magn. Reson. Med.*, vol. 2, pp. 428–436, 1985.
- [50] A. Alberts, *Regression and the Moore-Penrose Pseudoinverse*. New York: Academic, 1972.
- [51] A. Rosenfeld and A. C. Kak, *Digital Picture Processing*. New York, NY: Academic Press, 1982, ch. 8.
- [52] T. P. Trouard, R. J. Theilmann, M. I. Altbach, and A. F. Gmitro, "High resolution diffusion imaging with DIFRADFSE (diffusion-weighted radial acquisition of data with fast spin echo) MRI," *Magn. Reson. Med.*, vol. 42, pp. 11–18, 1999.
- [53] Z. H. Cho, O. Nalcioglu, H. W. Park, J. B. Ra, and S. K. Hilal, "Chemical-shift artifact correction scheme using echo-time encoding technique," *Magn. Reson. Med.*, vol. 2, pp. 253–261, 1985.